



# Regulation of band edge and specific surface area of $\text{Bi}_x\text{In}_y\text{OCl}$ microsphere for excellent photocatalytic performance

Yanguang Zhang<sup>a</sup>, Jing Tian<sup>a</sup>, Detong Tian<sup>a</sup>, Weibing Li<sup>a</sup>, Zhenze Liu<sup>b</sup>, Fenghui Tian<sup>b</sup>,  
Yuyu Bu<sup>c</sup>, Shaoping Kuang<sup>a,\*</sup>

<sup>a</sup> College of Environment and Safety Engineering, Qingdao University of Science and Technology, 53 Zhengzhou Road, Qingdao 266042, China

<sup>b</sup> Institute of Computational Science and Engineering, State Key Laboratory of Bio-Fibers and Eco-Textiles, College of Chemistry and Chemical Engineering, College of Environmental Science and Engineering, Qingdao University, Qingdao 266071, China

<sup>c</sup> Key Laboratory of Wide Band-Gap Semiconductor Materials and Devices, School of Microelectronics, Xidian University, Xi'an 710071, China



## ARTICLE INFO

### Article history:

Received 19 December 2020

Received in revised form 24 January 2021

Accepted 2 February 2021

Available online 5 February 2021

### Keywords:

$\text{BiInOCl}$

Solid solution

Photocatalytic performance

Energy band control

Sewage treatment

## ABSTRACT

In order to solve the problem of low efficiency of existing photocatalyst in wastewater treatment,  $\text{BiOCl}$  and  $\text{Bi}_x\text{In}_y\text{OCl}$  solid solution photocatalysts with different indium element content were prepared by one-step solvothermal method. The solid solution of indium element greatly affects the porous structure and specific surface area of  $\text{BiOCl}$ , and the specific surface area of  $\text{BiInOCl-0.5}$  is 9.26 times that of  $\text{BiOCl}$ , which provides abundant active sites for photocatalytic reaction. Furthermore, after indium element solid solution, the conduction band and valence band potentials of  $\text{BiOCl}$  shift towards negative and positive, respectively, enhancing the redox capacity of the photogenerated electrons and holes. Thus,  $\text{BiInOCl}$  shows excellent photocatalytic performances for reduction of  $\text{Cr(VI)}$ , degradation of norfloxacin, dyes and even industrial cotton pulp wastewater. This provides a possibility for the practical application of photocatalytic technology in industrial wastewater treatment.

© 2021 Elsevier B.V. All rights reserved.

## 1. Introduction

Photocatalysis is a potential technology in the field of energy and environment because of its pollution-free, low toxicity and the repeatability of photocatalysts, therefore it has been studied widely [1–3]. At present, the most widely studied photocatalysts include  $\text{TiO}_2$  [4,5],  $\text{ZnO}$  [6],  $\text{g-C}_3\text{N}_4$  [7–9],  $\text{CdS}$  [10,11],  $\text{BiVO}_4$  [12,13],  $\text{WO}_3$  [14],  $\text{BiOX}$  [15–17], etc. These semiconductor photocatalysts have been widely used in the degradation of dyes and antibiotic wastewater. However, the removal of refractory organic pollutants or treatment of industrial wastewater has been seldomly reported because their removal needs strong redox capability. Therefore, the design and synthesis of photocatalysts with high redox potential has become the key point to effectively remove refractory pollutants.

In recent years,  $\text{BiOX}$  ( $\text{X}=\text{Cl}, \text{Br}, \text{I}$ ) has attract wide attentions due to their unique layered structures that can form an built-in electric field to effectively avoid the recombination of photogenerated electrons and holes [18]. In addition, the band structure of  $\text{BiOX}$  semiconductors can be easily regulated by element solution, which

made the design of redox potential of the photogenerated charge carriers possible by adjusting the position of conduction band (CB) and valence band (VB) of  $\text{BiOX}$ . Specifically, two sites in the molecular structure of  $\text{BiOX}$ , the X and Bi sites, can be regulated by solid solution to modulate the band gap and energy band of  $\text{BiOX}$  [19]. For example, Jia et al. [20] realized a simultaneous control of CB and VB positions by adjusting the value of x in  $\text{BiOCl}_{1-x}\text{Br}_x$  ( $x=0, 0.5, 1$ ), the band gap changing from 3.37 eV ( $x=0$ ) to 2.92 eV ( $x=0.5$ ) and to 2.83 eV ( $x=1$ ). Lu et al. [21] also controlled the CB energy and band gap of  $\text{BiOBr}_x\text{I}_{1-x}$  by adjusting the x in  $\text{BiOBr}_x\text{I}_{1-x}$  ( $x=0-0.5$ ). In addition, the energy band of  $\text{BiOX}$  can also be regulated by solid solution of metal ions. It has been found that  $\text{Pb}^{2+}$  can be inserted between  $[\text{Bi}_2\text{O}_2]^{2+}$  layers, with Pb 6s<sup>2</sup> orbital occupying higher energy level at the top of VB, while Pb 6p orbital occupying lower energy level at the bottom of CB. The hybrid state of VB and CB can reduce the effective mass of holes and electrons [22], increasing the lifetime of excited carriers, and thus improve the photocatalytic activity.

Although the solid solution of the halogen atom can reduce the band gap of the semiconductor and broaden the photoresponse range, the redox potential of the photogenerated charge carriers would also be reduced. This is disadvantageous for total degradation, especially for the pollutants that need strong redox capability to

\* Corresponding author.

E-mail address: [kuangsp1120@126.com](mailto:kuangsp1120@126.com) (S. Kuang).

degrade. On the contrary, the widening of the semiconductor forbidden band within a certain range can increase the free radical energy and raise the degrade capability for complete degradation of pollutants, and thus has a better industrial application value. However, the work that increase the band gap and improve the redox ability of BiOX by solid solution has seldomly reported.

In this paper, the  $\text{Bi}_x\text{In}_y\text{OCl}$  photocatalysts were prepared by solid solution the indium (In) element into BiOCl using a one-step solvothermal method. The In element and Bi element are located in adjacent periods and have the same chemical valence, and the atomic radius of In is slightly smaller than Bi. Thus, lattice distortion is very likely to occur due to the mismatch of atomic radius in the solid solution process. In addition, In element is easily hydrolyzed to form a local acidic environment, which would change the local kinetics of the growth reaction, and thus has the possibility of modulating the microscopic morphology. More importantly, In element has the advantage of low toxicity. The solid solution of In element greatly increases the specific surface area of BiOCl, which endows it with more active sites. Meanwhile, after In element solid solution, the CB and VB potentials of BiOCl shift towards negative and positive, respectively, enhancing the redox capacity of the photo-generated electrons and holes. Therefore,  $\text{Bi}_x\text{In}_y\text{OCl}$  photocatalysts can rapidly degrade norfloxacin (NOR), dyes, Cr (VI) and Industrial cotton pulp wastewater (ICPW). This work provides a possibility for the practical application of photocatalytic technology in industrial wastewater treatment.

## 2. Experimental details

### 2.1. Materials

All the reagents were purchased from Aladdin Industrial Corporation (Shanghai, China), and all the reagents were directly used without purification.

#### 2.1.1. Synthesis of BiOCl

The BiOCl photocatalyst was prepared by Tian et al.[23]. In a typical synthesis of BiOCl materials, 4 mmol  $\text{Bi}(\text{NO}_3)_3 \cdot 5\text{H}_2\text{O}$  were dissolved into 80 mL ethylene glycol containing 4 mmol HCl solution. Then the mixture solution was further stirred for 30 min at room temperature to completely dissolving, and the above solution was transferred to a 100 mL Teflon-lined autoclave and heated at 140 °C for 24 h. After cooled down to room temperature, the samples were centrifuged and washed with distilled water and ethanol for several times to remove the inorganic and organic impurities. Finally, the sample was dried at 80 °C under air atmosphere. The obtained sample was labeled as BiOCl.

#### 2.1.2. Synthesis of $\text{Bi}_x\text{In}_y\text{OCl}$

For preparation  $\text{Bi}_x\text{In}_y\text{OCl}$  with different molar mass ratio of Bi:In, various amount of  $\text{In}(\text{NO}_3)_3 \cdot x\text{H}_2\text{O}$  and 4 mmol  $\text{Bi}(\text{NO}_3)_3 \cdot 5\text{H}_2\text{O}$  (the molar mass ratio of Bi:In were 2, 1, 0.5 and 0.33) were dissolved into 80 mL ethylene glycol containing 4 mmol HCl solution. And other procedures kept the same as that of pure BiOCl preparation process. The samples were labeled as BiInOCl-2, BiInOCl-1, BiInOCl-0.5 and BiInOCl-0.33, respectively.

### 2.2. Characterization of the prepared photocatalysts

The microstructure of the prepared photocatalyst was characterized using scanning electron microscopy (SEM, JSM-6700F; JEOL, Tokyo, Japan) and field emission high resolution transmission electron microscopy (FE-HRTEM, Tecnai G2 F20, FEI Company, USA). The crystal structure of the prepared photocatalyst was analyzed using X-ray diffraction (XRD, D/MAX-2500/PC; Rigaku Co., Tokyo, Japan). Elemental composition and bonding information were

obtained by energy scattering spectroscopy (EDS, FEI Tecnai G20, FEI Company, USA) and X-ray photoelectron spectroscopy (XPS, Axis Ultra, Kratos Analytical Ltd., England). The optical absorption properties of the prepared photocatalyst were studied by UV-Vis diffuse reflectance spectroscopy (U-41000; HITACHI, Tokyo, Japan). The photoluminescence intensity of the prepared photocatalyst was measured by microfluorescence spectroscopy (PL, fluoro Max-4, HORIBA Jobin Yvon, France). Generation of free radical information were obtained by electron paramagnetic resonance (ESR, EMX-8/2.7, Bruker, Germany). The Brunauer-Emmett-Teller (BET, 3Flex, Micromeritics, USA) was used to determine the Brunauer-Emmett-Teller surface area. Elemental contents were measured by Inductively Coupled Plasma Mass spectrometer (ICP-MS, ICAP-QC, Thermo, China).

### 2.3. Photocatalytic degradation measurements

300 W xenon lamp (PLS-SXE300, Beijing Changtuo Co., Ltd., China) was used as the light source during the photocatalytic degradation tests, and the tests were carried out under white light illumination.

In a typical photocatalytic reduction of Cr(VI), 0.05 g photocatalysts were dispersed in 100 mL Cr(VI) solution (the source of Cr is  $\text{K}_2\text{Cr}_2\text{O}_7$ ) with a concentration of  $50 \text{ mg} \cdot \text{L}^{-1}$ . The Cr(VI) solution was stirred for 30 min to achieve adsorption-desorption equilibrium in the dark, after which the suspension was illuminated under white light. 5 mL suspension was withdrawn per 5 min, and was centrifuged to remove the photocatalyst for testing the absorbance of Cr (VI) by a visible spectrophotometer (722E, Shanghai spectrum instrument Co., Ltd., China) at 540 nm using diphenylcarbazide colorimetric method. In addition, condensate water was used to keep the system at constant temperature.

In a typical photocatalytic oxidation of norfloxacin (NOR), the concentration of NOR is  $10 \text{ mg} \cdot \text{L}^{-1}$ . The steps of adsorption and degradation are the same as those of photocatalytic reduction of Cr(VI), and the absorbance of NOR by the UV-Vis diffuse reflectance spectroscopy. The photocatalytic steps of dyes include Rhodamine B (RhB,  $10 \text{ mg} \cdot \text{L}^{-1}$ ), methyl orange (MO,  $10 \text{ mg} \cdot \text{L}^{-1}$ ), methylene blue (MB,  $10 \text{ mg} \cdot \text{L}^{-1}$ ) are also the same as that of photocatalytic reduction of Cr(VI), and the absorbances of RhB, MO and MB were determined at 554 nm, 465 nm and 664 nm, respectively. Industrial cotton pulp wastewater (ICPW) was diluted by 10 times to carry out the photocatalytic degradation test, the specific steps are the same as above but the sampling time is different (per 1 h in photocatalytic degradation of ICPW). Due to the complex composition of ICPW, the photocatalytic degradation performance of the photocatalyst was simply tested by colorimetry.

### 2.4. Photoelectrochemical and electrochemical measurements

The electrochemical and photoelectrochemical tests were carried out in a three-electrode system using an electrochemical workstation (CHI660D, Chenhua, Shanghai). The prepared photoelectrode, a Pt electrode and an Ag/AgCl (saturated KCl) electrode acted as the working electrode, the counter electrode and the reference electrode, respectively. All tests were carried out in 0.1 M  $\text{Na}_2\text{SO}_4$  solution. The variations of the photoinduced current density with time (i-t curve) were measured at the bias potential of 0 V (vs Ag/AgCl) during a 3-cycle visible light switching on and off. A 300 W xenon lamp was used as the light source. Electrochemical impedance spectroscopy (EIS) tests were carried out at open circuit potential over the frequency range between  $10^{-2}$  and  $10^5$  Hz, with an AC voltage magnitude of 5 mV. Mott-Schottky plots was measured at the potential range of 1.6–2.3 V and the frequency of 1000 Hz with an AC voltage magnitude of 5 mV.

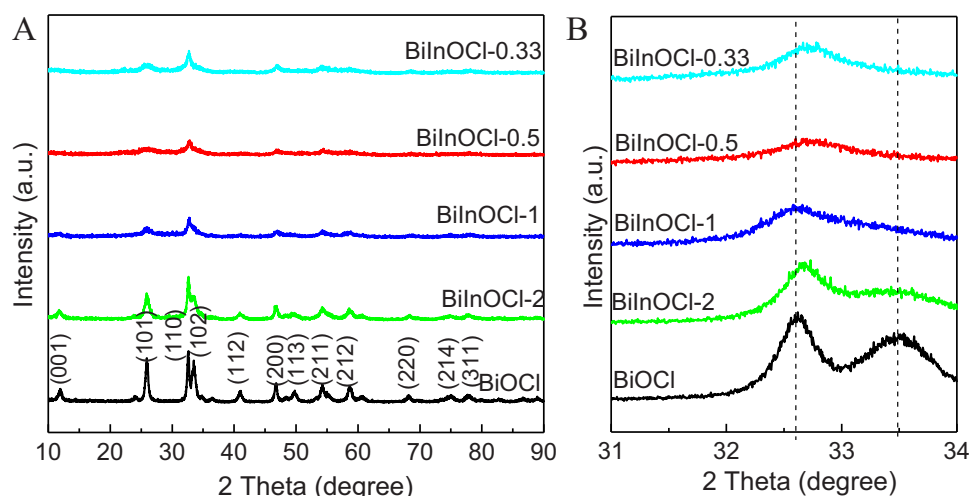


Fig. 1. XRD patterns(A) and XRD fine scanning patterns (B) of prepared BiOCl, BiInOCl-2, BiInOCl-1, BiInOCl-0.5 and BiInOCl-0.33.

## 2.5. Theoretical calculation

The BiInOCl bulk were simulated by a periodic ( $2 \times 2 \times 2$ ) slab model, as shown in Fig. S3. During the geometric optimization processes, the Monkhorst-Pack k-point mesh of  $3 \times 3 \times 1$  was adopted. DFT calculations were performed with the DMol<sup>3</sup> package in Material Studio. Exchange-correlation functional was constructed by Perdew-Bruke-Ernzerhof (PBE) of generalized gradient approximation (GGA). The double-numerical-quality basis set with polarization functions (DNP) was adopted to describe the valence orbital of the atoms. The core electrons were substituted by DFT semi-core pseudopotentials (DSPPs). The energy, force, and displacement convergence criteria were set to  $2.0 \times 10^{-5}$  hartree,  $4.0 \times 10^{-3}$  hartree/Å, and  $5.0 \times 10^{-3}$  Å, respectively.

## 3. Results and discussion

XRD was used to analyze the composition and phase of the photocatalyst, which was presented in Fig. 1A. In the XRD pattern of BiOCl, the XRD peaks at  $12^\circ$ ,  $25.9^\circ$ ,  $32.5^\circ$ ,  $33.4^\circ$ ,  $40.9^\circ$ ,  $46.6^\circ$ ,  $49.7^\circ$ ,  $54.1^\circ$ ,  $58.6^\circ$ ,  $68.1^\circ$ ,  $75^\circ$ ,  $78.8^\circ$  correspond to (001), (101), (110), (102), (112), (200), (113), (211), (212), (220), (214), (311) crystal faces of pure BiOCl, which comes from tetragonal BiOCl (PDF#06-0249) [24]. The  $\text{Bi}_x\text{In}_y\text{OCl}$  solid solutions display similar XRD pattern with the pristine BiOCl due to similar tetragonal structures. It is worth noting that the peak intensity ratio of (110) to (102) of the BiInOCl-2 sample is significantly higher than that of pure BiOCl, and the double peaks of (110) and (102) of BiInOCl-1 become an asymmetrical single peak with the increase of In element content. This phenomenon indicates that the  $\text{Bi}_x\text{In}_y\text{OCl}$  sample grows along the (110) crystal face after the addition of In element [25]. Hao et al. [26] have synthesized BiOCl with different morphologies and exposed facets by a simple solvothermal method, and found that the BiOCl microsphere with (110) facet exposing presented excellent photocatalytic activity. In addition, as the In element ratio continues to increase, the peak positions of BiInOCl-0.5 and BiInOCl-0.33 at  $2\theta = 32.6^\circ$  shift to larger angle (as shown in Fig. 1B). This is because the atomic radius of  $\text{In}^{3+}$  is smaller than that of  $\text{Bi}^{3+}$ , which causes the peak position to shift to a large angle [27,28]. In addition to the diffraction peak of BiOCl, the diffraction peak of  $\text{In}_2\text{O}_3$  did not appear in the XRD patterns, indicating that In element was fully dissolved in BiOCl. There are no other impurity peaks in the XRD patterns, which also indicates that the BiOCl and  $\text{Bi}_x\text{In}_y\text{OCl}$  samples prepared were pure single-phase structures.

The microscopic morphology of the prepared photocatalysts can be characterized by SEM technology. The SEM image of pure BiOCl is shown in Fig. 2A. BiOCl presents a microsphere structure with smooth surface and particle size of about 5–7  $\mu\text{m}$ . For the sample of BiInOCl-2 (Fig. 2B), the surface of the microspheres is still smooth, and the surface becomes irregular and the particle size is slightly reduced. BiInOCl-1 exhibits a distinct core-shell structure, as shown in Fig. 2C. The size of BiInOCl-1 microspheres becomes non-uniform and the surface changes to fluffs. With the doping content of In element increasing, the surface of BiInOCl-0.5 in Fig. 2D exhibits a rough porous structure, and the particle size is further reduced. Further adding the doping content of In element, as shown in Fig. 2E, the surface of BiInOCl-0.33 is still a rough porous structure, and the particle size is further reduced to 2–3  $\mu\text{m}$ .

High-resolution TEM was further performed in order to confirm the successful formation of In element solid solution. The low-resolution TEM image of BiOCl in Fig. 3A presents the microsphere structure of BiOCl. The edge of BiOCl microspheres is shown in Fig. 3B, where Lattice fringes of  $d = 0.195 \text{ nm}$  and  $d = 0.22 \text{ nm}$  corresponding to the (200) and (112) crystal planes of BiOCl, respectively can be observed. In Fig. 3C, BiInOCl-0.5 exhibits a structure with a tight core and a loose shell core. Only lattice fringe of  $d = 0.31 \text{ nm}$  exists in the high-resolution TEM images of Fig. 3D and Fig. 3E, indicating that the BiInOCl-2 sample does have crystal phase-oriented growth, which is consistent with the XRD results.

The elemental composition of BiInOCl-0.5 can be characterized by EDS under TEM. In element is also present in Fig. 2F in addition to the Bi, O and Cl elements, which confirmed the successful solid solution of In element. In addition, the EDS element mapping results under transmission electron microscopy in Fig. 3F indicate that BiInOCl-0.5 samples contain elements of Bi, In, O and Cl, and they are evenly distributed in BiInOCl-0.5 samples. This also confirmed the successful preparation of  $\text{Bi}_x\text{In}_y\text{OCl}$  solid solution. The elemental contents of Bi and In in the series of photocatalysts can be tested by ICP-MS, and the relevant data is shown in Table S1. It can be seen from Table S1 that as the added amount of In element increases, the content of Bi in  $\text{Bi}_x\text{In}_y\text{OCl}$  decreases, and the content of In element increases. The molar mass ratios of Bi:In in BiInOCl-2, BiInOCl-1, BiInOCl-0.5 and BiInOCl-0.33 are 6.33, 3.22, 1.39 and 1.19 respectively. From the ratio value of Bi:In, it can be seen that as the added amount of In element increases proportionally, the amount of In element in  $\text{Bi}_x\text{In}_y\text{OCl}$  also increases proportionally, indicating that In element has successfully replaced Bi in the solid solution process.

XPS of BiOCl and BiInOCl-0.5 were tested to confirm their elemental composition and chemical state. The total spectra of BiOCl



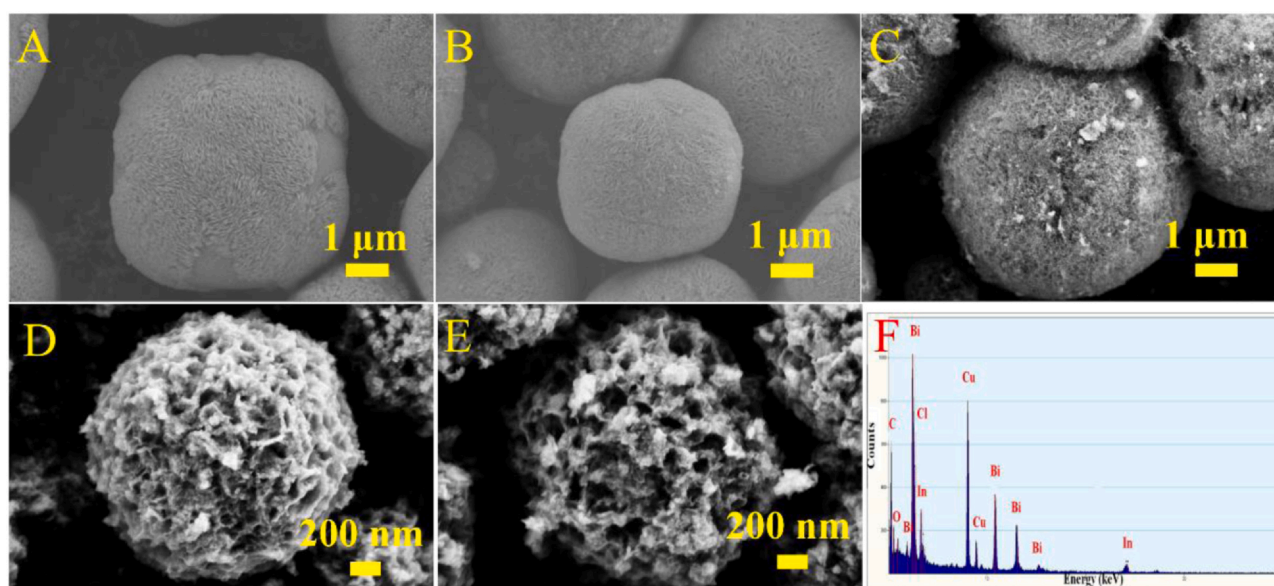


**Fig. 2.** SEM images of (A) BiOCl, (B) BiInOCl-2, (C) BiInOCl-1, (D) BiInOCl-0.5, (E) BiInOCl-0.33 and (F) the EDS of BiInOCl-0.5.

and BiInOCl-0.5 in Fig. S1 show the existence of Bi, O, Cl elements in BiOCl and Bi, In, O, Cl in BiInOCl-0.5 without any other impurity element, which are consistent with the above-mentioned results of EDS and EDS element mapping. XPS of Bi4f is shown in Fig. 4A where peaks at 159.38 eV and 164.69 eV are observed, which can be ascribed to Bi4f<sub>7/2</sub> and Bi4f<sub>5/2</sub> [29], respectively, that come from to Bi<sup>3+</sup>. Compared with pure BiOCl, the BiInOCl-0.5 sample has a larger

binding energy at Bi4f<sub>7/2</sub> and Bi4f<sub>5/2</sub>. This is owing to the fact that the solid solution of In element broke part of Bi-O bond [12], increasing the external electron density of Bi surface, thus increasing the binding energy. The XPS of Cl2p is shown in Fig. 4B, and the peaks at 198.1 eV and 199.7 eV correspond to Cl2p<sub>3/2</sub> and Cl2p<sub>1/2</sub> [30], respectively. The binding energy of Cl2p in BiInOCl-0.5 sample did not change significantly compared with that in BiOCl, indicating the

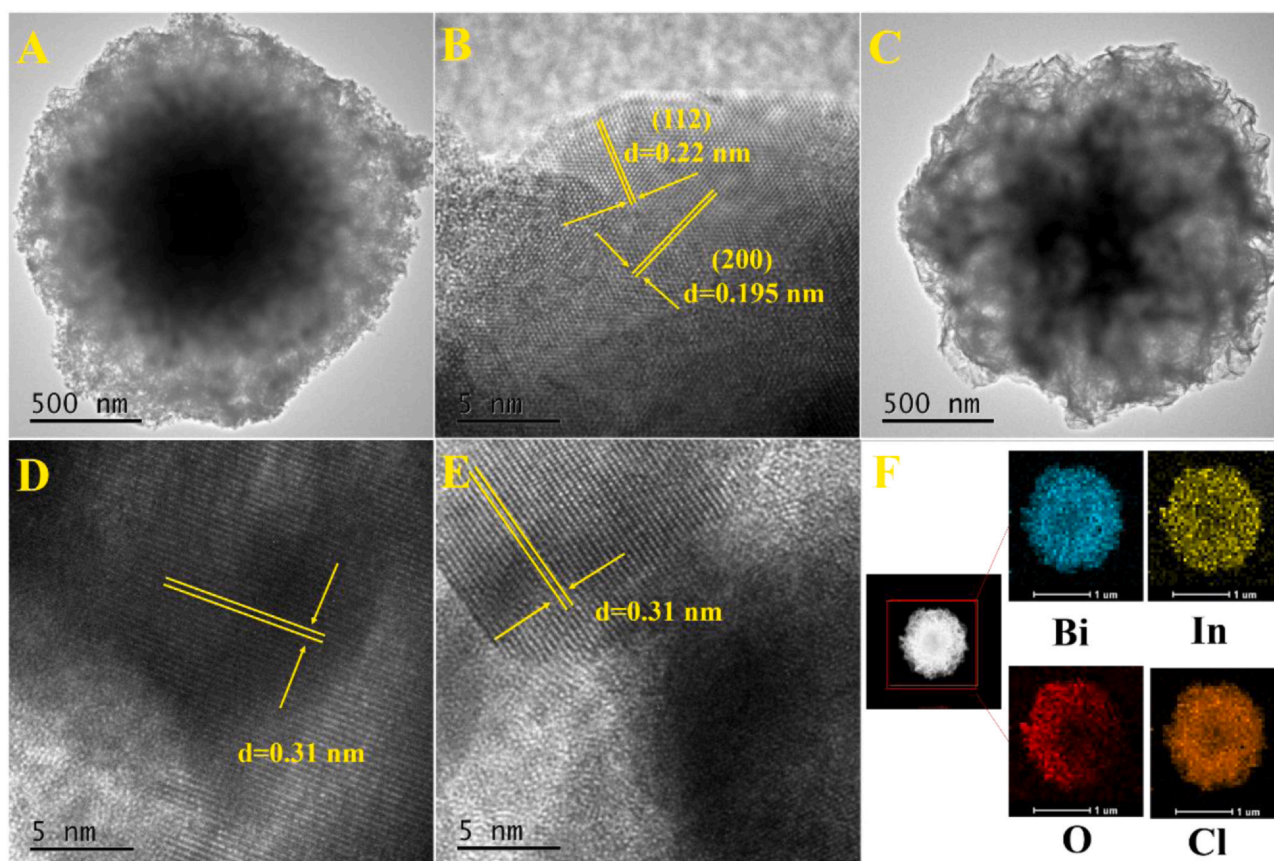


**Fig. 3.** TEM images of the prepared (A) low-resolution BiOCl; (B) high-resolution BiOCl; (C) low-resolution BiInOCl-1; (D) and (E) high-resolution BiInOCl-0.5; (F) EDS element mappings of BiInOCl-0.5.

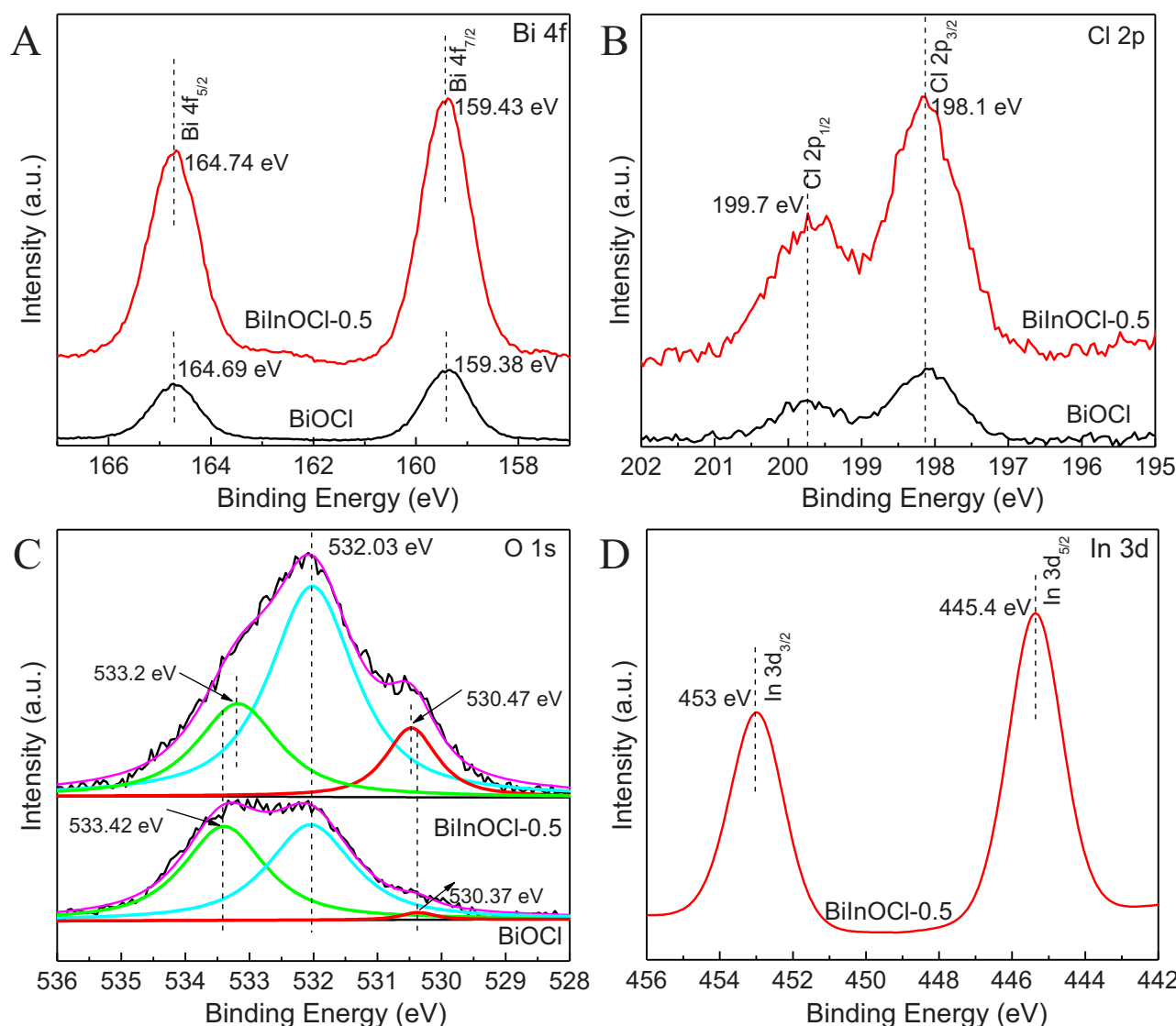


**Fig. 4.** XPS spectra of samples BiOCl and BiInOCl-0.5. (A) the Bi4f XPS core level spectrum; (B) the Cl2p XPS core level spectrum; (C) the O1s XPS core level spectrum, (D) the In3d XPS core level spectrum.

unchanging chemical state of Cl. As shown in Fig. 4C, three binding energies located at 530.37 eV, 532.03 eV and 533.2 eV are obtained, illustrating that the existence of three states of oxygen in the BiOCl sample. The binding energies at 530.37 eV, 532.03 eV, and 533.2 eV are corresponding to the binding energy of lattice oxygen Bi-O in BiOCl, adsorption hydroxyl group and adsorbed water molecule [31]. In Fig. 4D, the peaks at 445.4 eV and 453 eV correspond to the binding energy of In3d<sub>5/2</sub> and In3d<sub>3/2</sub>, respectively, indicating the existence of In element in BiOCl.

The BET specific surface area of the photocatalysts were tested by the N<sub>2</sub> adsorption-desorption isotherm (as shown in Fig. 5A). The classification of physical adsorption isotherms and hysteresis rings proposed by IUPAC show that the adsorption/desorption isotherms of the series photocatalysts are IV-type, indicating that the samples have mesoporous structure [4]. The specific surface areas of BiOCl is 11.02 m<sup>2</sup>/g. The specific surface areas of BiInOCl-2, BiInOCl-1, BiInOCl-0.5 and BiInOCl-0.33 increase to 25.02 m<sup>2</sup>/g, 71.32 m<sup>2</sup>/g, 102.03 m<sup>2</sup>/g and 75.84 m<sup>2</sup>/g, respectively, indicating that the solid solution of In can significantly adjust the surface area of the Bi<sub>x</sub>In<sub>y</sub>OCl photocatalyst. Larger specific surface area will provide more active sites for photocatalytic reaction, which is conducive to

the photocatalytic reaction. Fig. 5B shows the UV-Vis diffuse reflectance spectra results of the prepared photocatalyst, from which the light absorption threshold of BiOCl is observed at approximately 388 nm. The light absorption thresholds of Bi<sub>x</sub>In<sub>y</sub>OCl show blue shift compared with that of BiOCl. This indicates that the solid solution of In element cause the decrease of absorption range of BiOCl. That is to say, the conduction band or valence band of BiOCl is changed, thus affecting the redox ability.

Photocatalytic reduction of Cr(VI) was carried out under white light to assess the photocatalytic performances of the prepared photocatalysts, and the relevant results are shown in Fig. 6. Fig. 6A shows the photocatalytic reduction efficiency curves over Cr(VI). Before photocatalytic reduction under white light illumination, the adsorption-desorption equilibrium was achieved in dark for 30 min. The blank experiment in Fig. 6A shows that Cr(VI) can not be reduced without photocatalyst under white light illumination. The photocatalytic reduction efficiency of BiOCl for Cr(VI) is only 18.80% in 60 min. With the increase of In, the photocatalytic reduction efficiency of BiOCl gradually increases, and BiInOCl-0.5 shows the highest photocatalytic reduction efficiency which can reach 99.05% in 40 min. Fig. 6B shows the digital photos of Cr(VI) after 0 min,

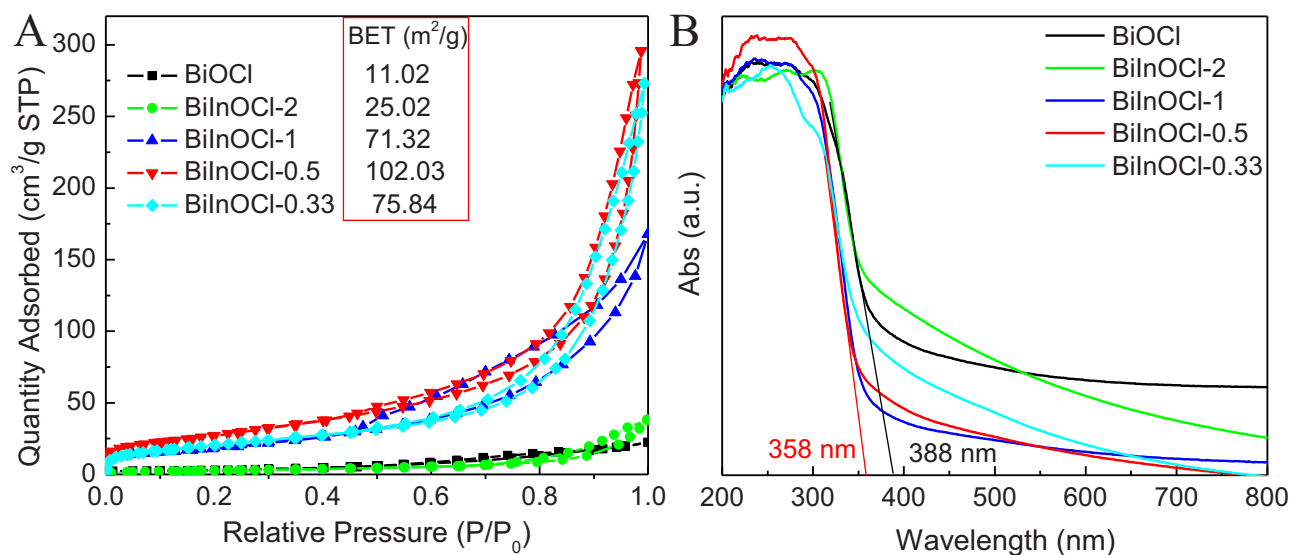


Fig. 5. (A) The nitrogen adsorption/desorption isotherms and (B) UV-Vis diffuse reflectance spectra of the prepared BiOCl, BiInOCl-2, BiInOCl-1, BiInOCl-0.5 and BiInOCl-0.33.

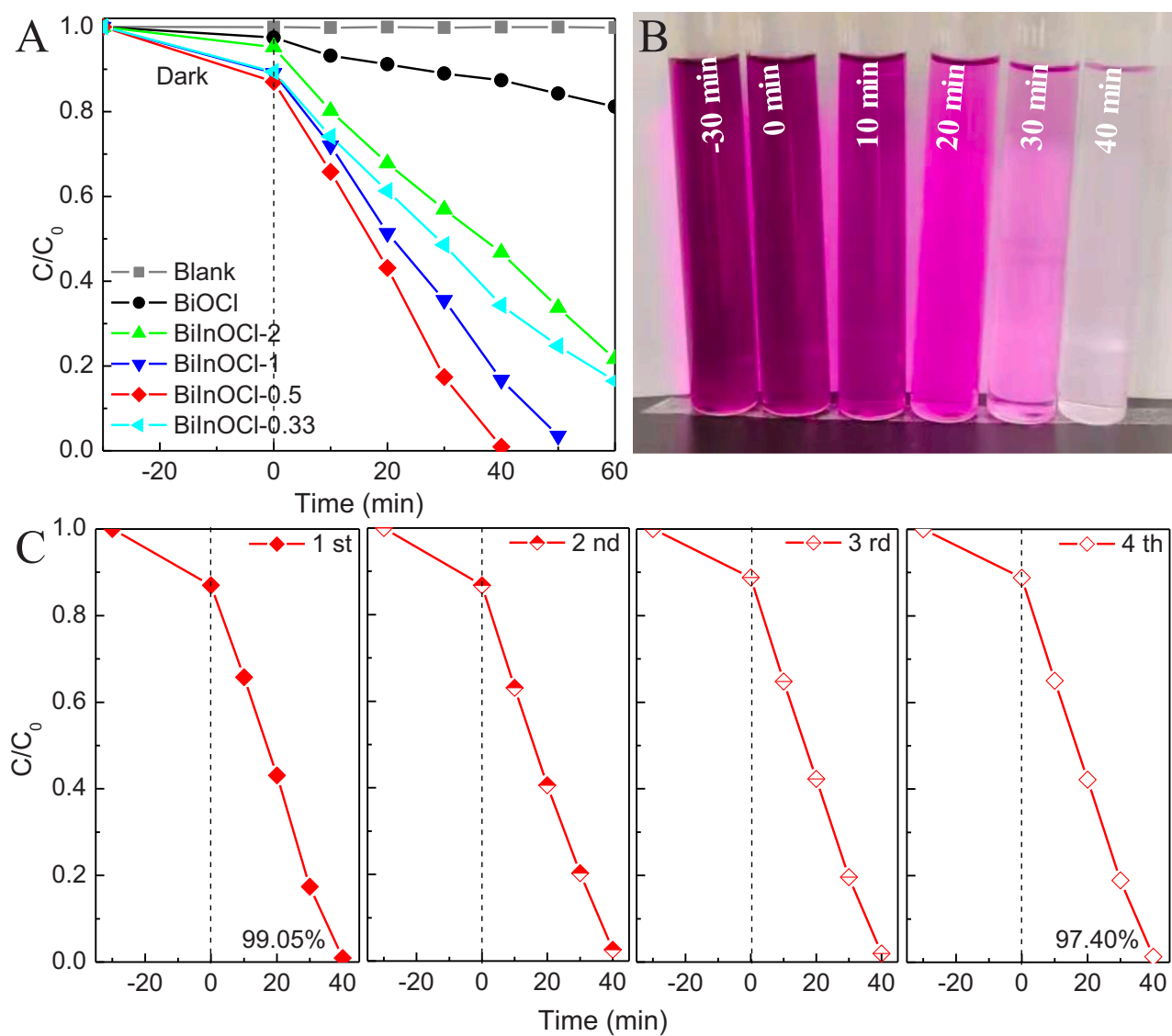
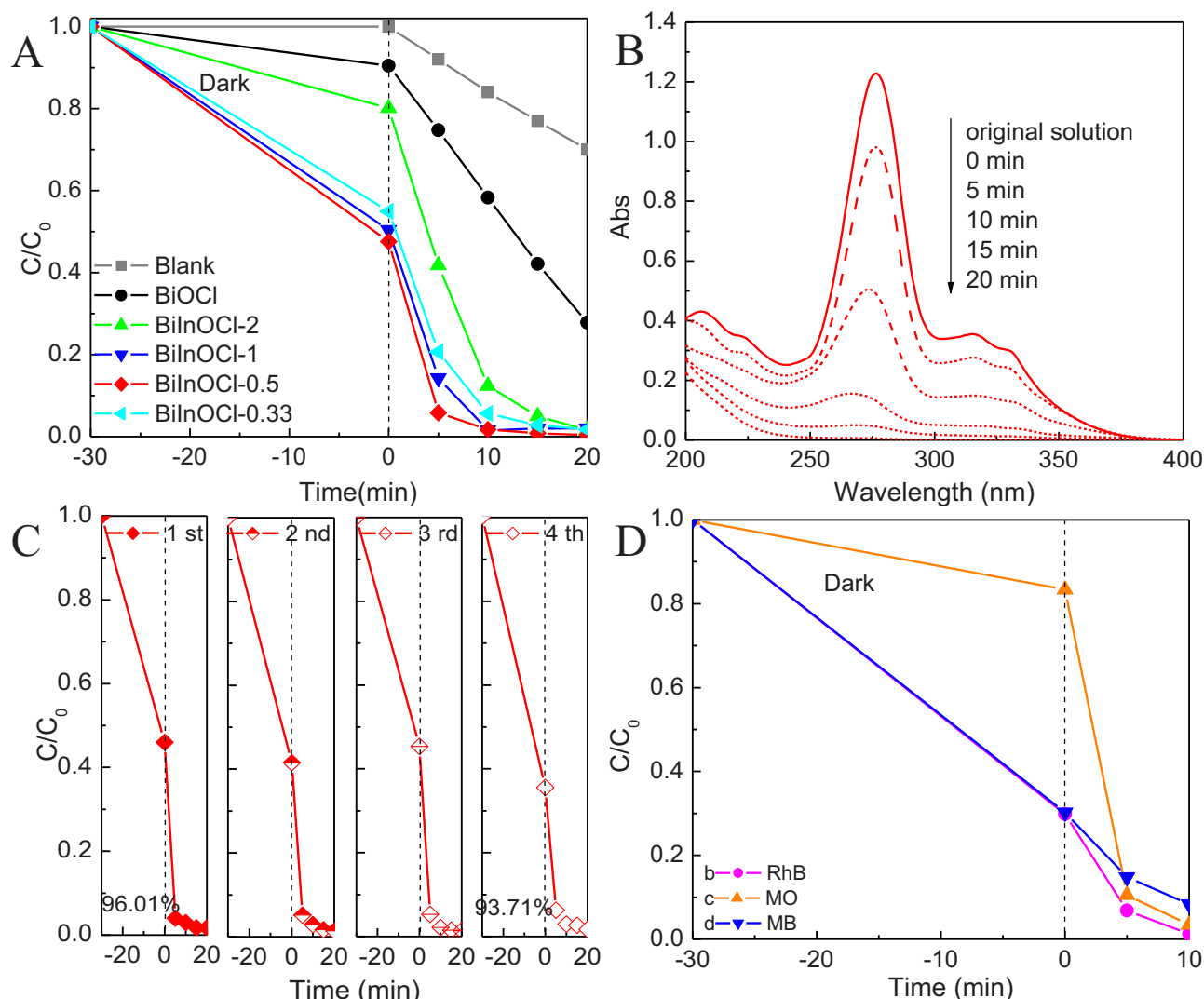


Fig. 6. (A) Photocatalytic performances of the prepared photocatalysts for Cr(VI) (50 mg/L) reduction under white light illumination. (B) The digital photos of Cr(VI) after different time of treatment by BiInOCl-0.5. (C) The stability test of photocatalytic reduction of Cr(VI) by BiInOCl-0.5.



**Fig. 7.** (A) Photocatalytic degradation NOR under white light illumination. (B) UV-vis spectrum of NOR degradation reaction of BiInOCl-0.5. (C) The stability test of photocatalytic degradation of NOR of BiInOCl-0.5. (D) Photocatalytic degradation RhB, MO and MB performance of BiInOCl-0.5 under white light illumination.

10 min, 20 min, 30 min, 40 min treatment by BiInOCl-0.5. With the further increase of In, the photocatalytic removal performance of BiInOCl-0.33 decreased, which may be ascribed to the decrease of active sites caused by the destruction of the porous structure of  $\text{Bi}_x\text{In}_y\text{OCl}$  microspheres. Fig. 6C shows the stability test of BiInOCl-0.5 for photocatalytic reduction of Cr(VI). It is found that the photocatalytic reduction efficiency of BiInOCl-0.5 only decreased by 1.65% after four cycles, indicating that BiInOCl-0.5 has a good photocatalytic degradation stability for Cr(VI).

In order to study the photocatalytic oxidation performances of the prepared photocatalysts, the performances of photocatalytic degradation for NOR under white light illumination were further performed. Fig. 7A presents the results of photocatalytic degradation for NOR. The adsorption and degradation properties of  $\text{Bi}_x\text{In}_y\text{OCl}$  are greatly improved, and BiInOCl-0.5 shows the best adsorption and photocatalytic degradation performance. The improvement of adsorption performance can be attributed to the increased specific surface area of  $\text{Bi}_x\text{In}_y\text{OCl}$  as shown in Fig. 5A. The larger specific surface area provides more active sites for the adsorption and degradation of the reactants [32,33]. The  $\text{Bi}_x\text{In}_y\text{OCl}$  can degrade NOR by 96% in 5 min, while the BiOCl only reaches 23%. Fig. 7B presents the UV-vis spectrum of NOR degradation reaction of BiInOCl-0.5. With the degradation time increasing, the NOR characteristic peaks of

aromatic rings [34] at 275 nm and that of piperazine [35] at 325 nm decrease gradually until disappear, with no other peaks appeared. It can be seen from Fig. 7B that the characteristic peak of NOR has a slight shift, this indicates intermediate product produced during degradation. But with the extension of the degradation time, the characteristic peak disappears, which indicates that NOR is completely degraded. The photocatalytic degradation of BiInOCl-0.5 was tested for four cycles to study its photocatalytic stability, as shown in Fig. 7C. The adsorption performance in the second, third and fourth cycles are higher than that in the first cycle, indicating that the NOR adsorbed on the surface of the photocatalyst can be completely degraded without affecting reuse of the photocatalyst. It is worth noting that the degradation performance after four cycles of degradation only decreased by 2.3%. Therefore, BiInOCl-0.5 has not only good degradation performance, but also good degradation stability, which is crucial to its further application. In order to study the degradation selectivity of  $\text{Bi}_x\text{In}_y\text{OCl}$ , BiInOCl-0.5 was further selected to degrade RhB, MO and MB, and the results are shown in Fig. 7D. The results indicate that for whether NOR or colored dyes, BiInOCl-0.5 exhibit excellent adsorption and photocatalytic degradation performance.

In addition, the prepared photocatalysts also have good photocatalytic removal performances for industrial wastewater that is



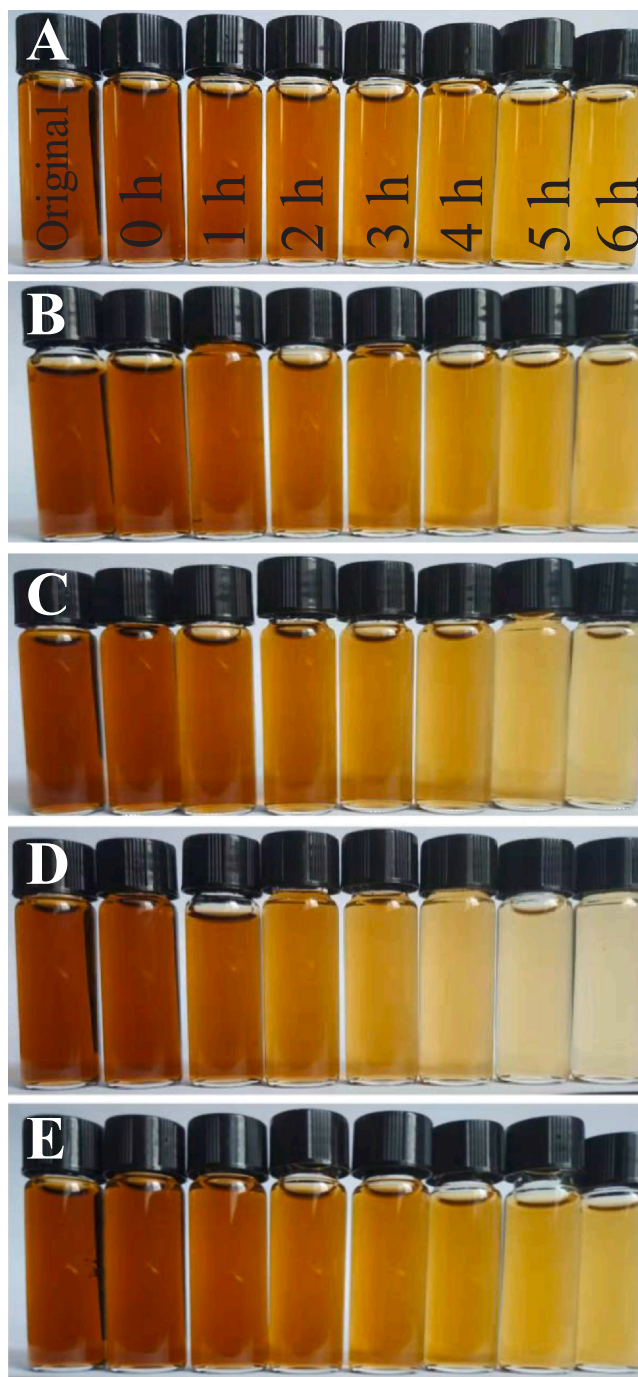


**Fig. 8.** Actual photos of cotton pulp mill wastewater after 0 h, 1 h, 2 h, 3 h, 4 h, 5 h, 6 h treatment over (A) BiOCl, (B) BiInOCl-2, (C) BiInOCl-1, (D) BiInOCl-0.5, (E) BiInOCl-0.33.

difficult to degrade. Fig. 8 shows the digital photos of cotton pulp mill wastewater after treatment of 0 h, 1 h, 2 h, 3 h, 4 h, 5 h and 6 h by the prepared photocatalysts. All the prepared photocatalysts have certain removal effect on cotton pulp wastewater, but the removal efficiency of BiInOCl-0.5 (Fig. 8D) is the most obvious. The BiInOCl-0.5 can completely decolorized the wastewater in about 6 h, indicating its considerable potential in the industrial wastewater treatment.

Transient photocurrent responses of the prepared BiOCl and BiInOCl-0.5 samples were tested to study the separation efficiency of photogenerated electrons and holes. As shown in Fig. S2A, the

photogenerated current density of BiInOCl-0.5 is obviously higher than that of BiOCl, which indicates that the solid solution of In element improve the separation of photogenerated charge carriers and thus enhance the photocatalytic performance. It can be seen from the Fig. S2A that the photocurrent curves of BiInOCl-0.5 and BiOCl are opposite. This is because the addition of In changes BiOCl from a p-type semiconductor to an n-type semiconductor of BiInOCl, which makes the photocurrent curve opposite. In the EIS results shown in Fig. S2B, the impedance arc radius of BiInOCl-0.5 is smaller than that of BiInOCl-0.5, indicating the higher interfacial charge transfer ability of BiInOCl-0.5.

ESR tests of free radicals were carried out in order to study the reasons for the improvement of photocatalytic performances, and the corresponding results are shown in Fig. 9. Figs. 9A and 9B show the results of  $\cdot\text{O}_2^-$  in the dark and after exposure to white light for 4 min, respectively. Figs. 9C and 9D present the results of  $\cdot\text{OH}$  in the dark and after exposure to white light for 4 min, respectively. No signal is found in Fig. 9A and Fig. 9C, indicating that  $\cdot\text{O}_2^-$  and  $\cdot\text{OH}$  can't be generated in the dark. On the contrary, the signal of  $\cdot\text{O}_2^-$  with intensity ratio of 1:1:1:1, as shown in Fig. 9B, and the signal of  $\cdot\text{OH}$  with intensity ratio of 1:2:2:1, as shown in Fig. 9D, were generated when illuminated for 4 min, which indicates that  $\cdot\text{O}_2^-$  and  $\cdot\text{OH}$  were produced in both BiOCl and BiInOCl-0.5 samples under illumination. Moreover, the signal intensities of  $\cdot\text{O}_2^-$  and  $\cdot\text{OH}$  from BiInOCl-0.5 sample are stronger than those from BiOCl, indicating that BiInOCl-0.5 can generate more  $\cdot\text{O}_2^-$  and  $\cdot\text{OH}$ . Therefore, BiInOCl-0.5 has stronger photocatalytic redox capability and thus better photocatalytic degradation performances.

Band gap width and Mott-Schottky were tested in order to study the energy band change of BiOCl and  $\text{Bi}_x\text{In}_y\text{OCl}$ . Fig. 10A was transformed from Fig. 5B, from which we can obtain that the band gaps of BiOCl, BiInOCl-2, BiInOCl-1, BiInOCl-0.5 and BiInOCl-0.33 are 3.19, 3.27, 3.36, 3.45 and 3.31 eV, respectively. Fig. 10B presents the Mott-Schottky test of BiOCl and  $\text{Bi}_x\text{In}_y\text{OCl}$ , in which all the slopes are negative, indicating that all of them are p-type semiconductors. At the same time, according to the intersection of the linear part and the abscissa in Mott-Schottky, the flat band potentials of BiOCl, BiInOCl-2, BiInOCl-1, BiInOCl-0.5 and BiInOCl-0.33 are 1.98, 2.04, 2.09, 2.15 and 2.12 V (vs Ag/AgCl), respectively. Because the flat band potential of p-type semiconductors is approximately equal to its VB potential, the VB potentials of BiOCl, BiInOCl-2, BiInOCl-1, BiInOCl-0.5 and BiInOCl-0.33 are 1.98, 2.04, 2.09, 2.15 and 2.12 V (vs Ag/AgCl), respectively. The VB potential, CB potential and band gap of a semiconductor material have the following relationship:

$$E_g = E_{VB} - E_{CB}(1)$$

where,  $E_{VB}$  is the VB potential of the semiconductor material,  $E_g$  is the band gap of the semiconductor material, and  $E_{CB}$  is the CB potential of the semiconductor material. Therefore, the CB potentials of BiOCl, BiInOCl-2, BiInOCl-1, BiInOCl-0.5 and BiInOCl-0.33 can be calculated based on Formula (1), and they are -1.01, -1.03, -1.07, -1.10 and -0.99 V (vs Ag/AgCl), respectively. According to Fig. 10A, Fig. 10B and the CB potentials calculated by Formula (1), the band structure diagram is drawn as shown in Fig. 10C. According to the above analysis, the solid solution of In element can not only increase the band gap of BiOCl, but also positively shift the VB and negatively shift the CB. BiInOCl-0.5 has the most negative CB potential and the most positive VB potential, thus BiInOCl-0.5 photocatalyst has the strongest redox ability. A possible mechanism diagram of BiInOCl-0.5 with better photocatalytic performance is illustrated in Fig. 10D. Firstly, BiInOCl-0.5 exhibits a porous structure and a larger specific surface area, thereby providing more active sites for surface reactions. Secondly, BiInOCl-0.5 has a wide band gap (3.35 eV), and the negative CB potential and the positive VB potential lead to stronger reduction and oxidation capacity. Due to the strong redox potential



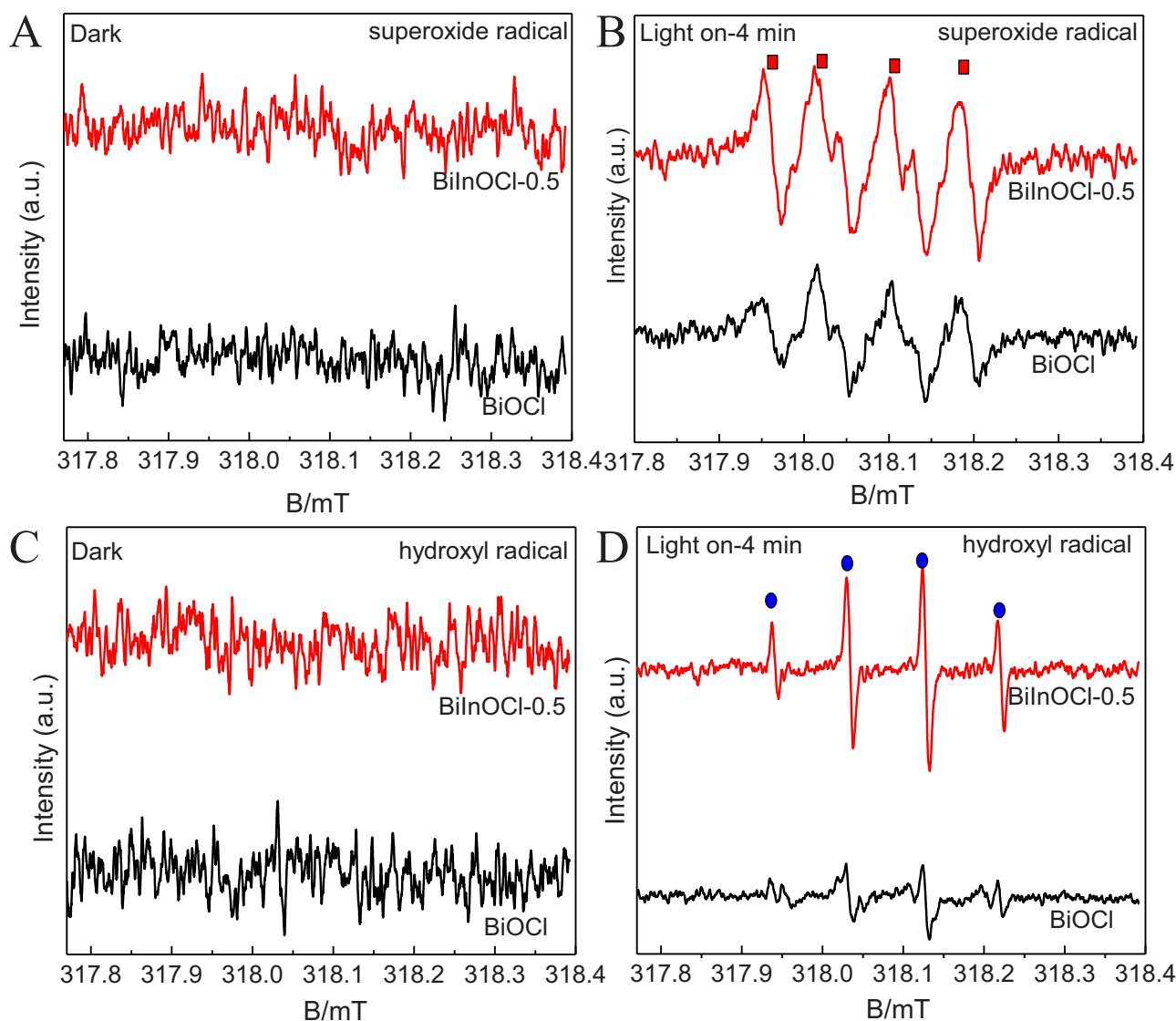


**Fig. 9.** DMPO spin-trapping ESR spectra recorded with the  $BiOCl$  and  $BiInOCl-0.5$  samples in (A), (B) methanol dispersion (for  $DMPO-O_2^{\cdot-}$ ) and (C), (D) aqueous dispersion (for  $DMPO-OH$ ) under white light irradiation.

of the photogenerated charge carriers,  $BiInOCl-0.5$  can efficiently reduce toxic  $Cr(VI)$  to  $Cr(III)$  and degrade NOR, RhB, MO, MB and ICPW etc. to small molecules of carbon dioxide and water.

To investigate the effect of solid solution of In on the band gap of  $BiOCl$ , we further calculated the band structure of  $BiOCl$  before and after In doping by DFT method. As shown in Fig. 11 A, the band gap can be calculated by the distance from the highest point between G and F to the G point. The band gap of  $BiOCl$  in this work is 2.65 eV, which matches well with the results of Zhang et al. [36]. After the solid solution of In ( $Bi:In=0.5$ ), as shown in Fig. 11 B, the band gap is 2.77 eV, which is 0.12 eV larger than that of  $BiOCl$ . The UV-Vis diffuse reflectance results show that the band gaps of pure  $BiOCl$  and  $BiInOCl-0.5$  are 3.20 eV and 3.35 eV, and the band gap difference before and after the solid solution of In is 0.15 eV. The calculation results are consistent with the experimental results.

Then we plotted the charge density difference of all atoms in the  $BiInOCl-0.5$  (001) plane to investigate the bonding behavior between the In atoms and the O atoms around them. As shown in Fig. 11 C, a significant covalent bond exists between In atoms and the O atoms. From the perspective of electron cloud overlap, the In-O covalent bond is much stronger than the Bi-O covalent bond. Therefore, it can

be inferred that the solid solution of In will cause a significant change in the electronic structure of  $BiOCl$ .

#### 4. Conclusion

In this paper,  $BiOCl$  and a series of  $Bi_xIn_yOCl$  solid solution photocatalysts with porous microsphere structure were prepared by a simple low-temperature solvothermal method. After In element solid solution in  $BiOCl$ , the porous structures and exposed facet of  $BiInOCl$  are changed to enlarge the specific surface area. Meanwhile, the CB and VB potentials of  $Bi_xIn_yOCl$  shift towards negative and positive, respectively, enhancing the redox capacity of the photogenerated electrons and holes. Thus,  $BiInOCl-0.5$  shows excellent performances for photocatalytic reduction of  $Cr(VI)$  and photocatalytic oxidation NOR, RhB, MO, MB and even industrial cotton pulp wastewater.

#### 5. CRediT authorship contribution statement

**Zhang Yanguang:** Methodology, Formal analysis, Investigation, Data curation, Writing - original draft. **Tian Jing:** Methodology, Writing - original draft. **Tian Detong:** Investigation, Visualization. **Li Weibing:**

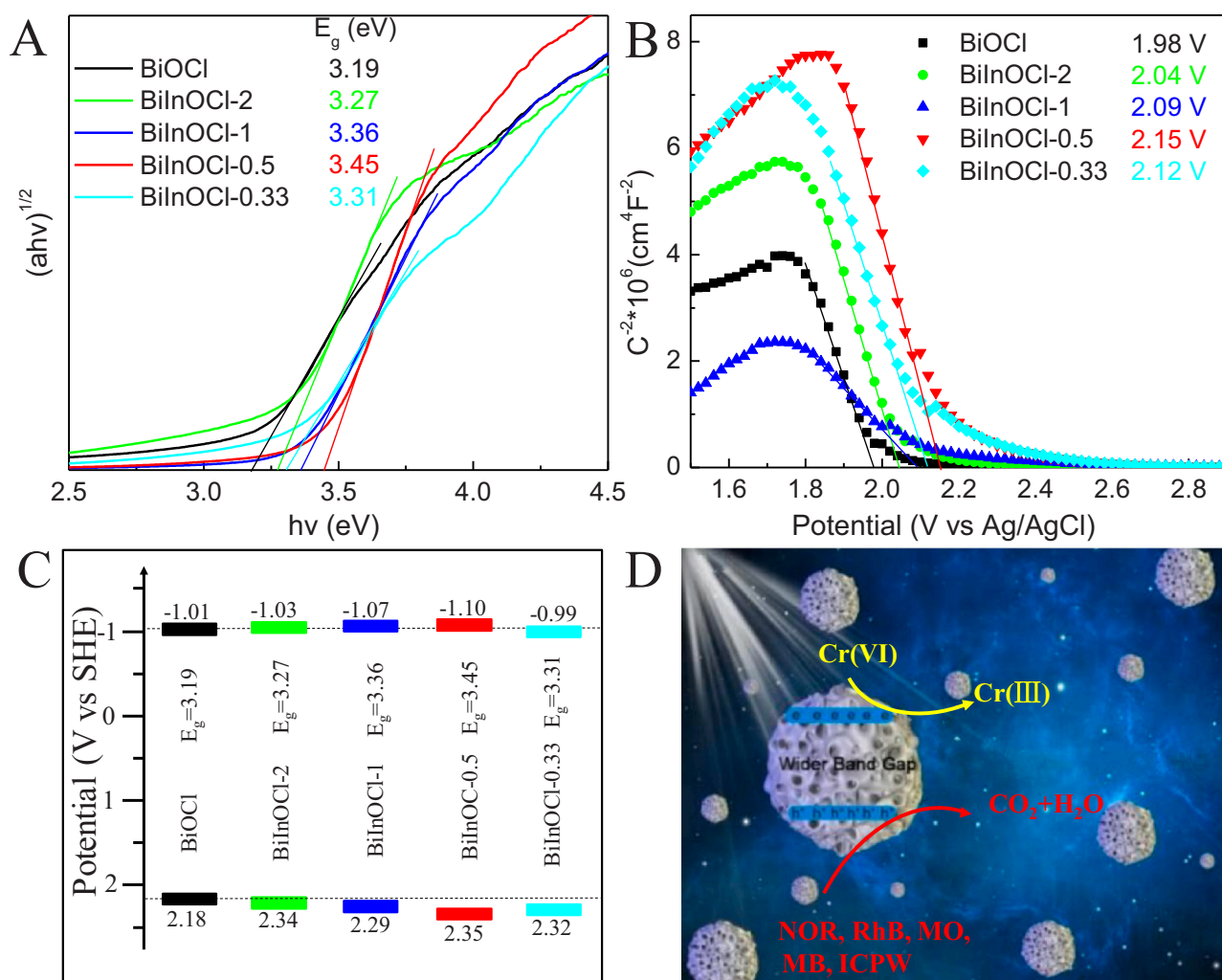


**Fig. 10.** (A) Band gap width of the prepared photoelectrodes obtained by Tauc plot formula, (B) Mott-Schottky, (C) the energy band structure diagrammatic sketch of prepared photoelectrodes, (D) Possible mechanism for improving photocatalytic performance of BiInOCl-0.5.

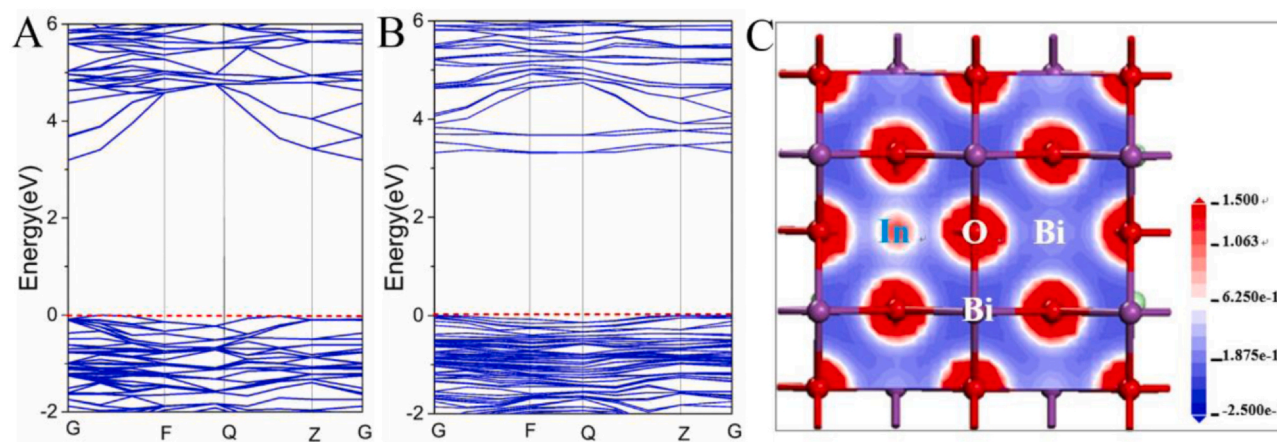


**Fig. 11.** (A) Band structure of pure BiOCl, (B) band structure of BiInOCl-0.5 and (C) the charge density difference of all the atoms for (001) plane of BiInOCl-0.5 crystal.

Conceptualization, Methodology, Resources, Writing - review & editing, Supervision. **Liu Zhenze:** Formal analysis, Visualization. **Tian Fenghui:** Methodology, Formal analysis, Resources. **Bu Yuyu:** Writing - review & editing. **Kuang Shaoping:** Conceptualization, Resources, Writing - review & editing, Funding acquisition.

#### Declaration of Competing Interest

The authors declare that they have no known competing financial interests or personal relationships that could have appeared to influence the work reported in this paper.

## Acknowledgements

This work was supported by the National Natural Science Foundation of China (41673112).

## Appendix A. Supporting information

Supplementary data associated with this article can be found in the online version at doi:10.1016/j.jallcom.2021.159052.

## References

- [1] Z. Cui, X. Dong, Y. Sun, Y. Zhou, Y. Zhang, F. Dong, Simultaneous introduction of oxygen vacancies and Bi metal onto the {001} facet of Bi<sub>2</sub>O<sub>3</sub>Cl woven nanobelts for synergistically enhanced photocatalysis, *Nanoscale* 10 (2018) 16928–16934.
- [2] S. Banerjee, S.C. Pillai, P. Falaras, K.E. O'shea, J.A. Byrne, D.D. Dionysiou, New insights into the mechanism of visible light photocatalysis, *J. Phys. Chem. Lett.* 5 (2014) 2543–2554.
- [3] H. Wang, W. Zheng, W. Li, F. Tian, S. Kuang, Y. Bu, J.-P. Ao, Control the energy band potential of ZnMgO solid solution with enhanced photocatalytic hydrogen evolution capacity, *Appl. Catal. B Environ.* 217 (2017) 523–529.
- [4] J. Yu, J. Low, W. Xiao, P. Zhou, M. Jaroniec, Enhanced photocatalytic CO<sub>2</sub>-reduction activity of anatase TiO<sub>2</sub> by coexposed {001} and {101} facets, *J. Am. Chem. Soc.* 136 (2014) 8839–8842.
- [5] J. Tian, Z. Chen, J. Jing, C. Feng, M. Sun, W. Li, Photoelectrochemical cathodic protection of Cu<sub>2</sub>O/TiO<sub>2</sub> pn heterojunction under visible light, *J. Oceanol. Limnol.* (2020) 1–15.
- [6] H. Wang, J. Tian, W. Li, Electrochemical deposition of MgO@ZnO shell- core nanorod arrays largely enhances the photoelectrochemical water splitting performance, *ChemElectroChem* 4 (2017) 2019–2026.
- [7] Y. Deng, L. Tang, G. Zeng, Z. Zhu, M. Yan, Y. Zhou, J. Wang, Y. Liu, J. Wang, Insight into highly efficient simultaneous photocatalytic removal of Cr (VI) and 2, 4-dichlorophenol under visible light irradiation by phosphorus doped porous ultrathin g-C<sub>3</sub>N<sub>4</sub> nanosheets from aqueous media: performance and reaction mechanism, *Appl. Catal. B Environ.* 203 (2017) 343–354.
- [8] J. Tian, Z. Chen, J. Jing, C. Feng, M. Sun, W. Li, Enhanced photocatalytic performance of the MoS<sub>2</sub>/g-C<sub>3</sub>N<sub>4</sub> heterojunction composite prepared by vacuum freeze drying method, *J. Photochem. Photobiol. A Chem.* 390 (2020) 112260.
- [9] H. Wang, G. Huang, Z. Chen, W. Li, Carbon self-doped carbon nitride nanosheets with enhanced visible-light photocatalytic hydrogen production, *Catalysts* 8 (2018) 366.
- [10] C. Feng, Z. Chen, J. Hou, J. Li, X. Li, L. Xu, M. Sun, R. Zeng, Effectively enhanced photocatalytic hydrogen production performance of one-pot synthesized MoS<sub>2</sub> clusters/CdS nanorod heterojunction material under visible light, *Chem. Eng. J.* 345 (2018) 404–413.
- [11] Z. Ji, H. Wang, X. She, A novel CdS quantum dots decorated 3D Bi<sub>2</sub>O<sub>3</sub>CO<sub>3</sub> hierarchical nanoflower with enhanced photocatalytic performance, *Catalysts* 10 (2020) 1046.
- [12] Y. Bu, J. Tian, Z. Chen, Q. Zhang, W. Li, F. Tian, J.P. Ao, Optimization of the photoelectrochemical performance of Mo-doped BiVO<sub>4</sub> photoanode by controlling the metal-oxygen bond state on (020) facet, *Adv. Mater. Interfaces* 4 (2017) 1601235.
- [13] Y. Zhang, Y. Li, D. Ni, Z. Chen, X. Wang, Y. Bu, J.P. Ao, Improvement of BiVO<sub>4</sub> photoanode performance during water photo-oxidation using Rh-doped SrTiO<sub>3</sub> perovskite as a co-catalyst, *Adv. Funct. Mater.* 29 (2019) 1902101.
- [14] Y. Bu, J. Ren, H. Zhang, D. Yang, Z. Chen, J.-P. Ao, Photogenerated-carrier separation along edge dislocation of WO<sub>3</sub> single-crystal nanoflower photoanode, *J. Mater. Chem. A* 6 (2018) 8604–8611.
- [15] H. Cheng, B. Huang, Y. Dai, Engineering BiOX (X=Cl, Br, I) nanostructures for highly efficient photocatalytic applications, *Nanoscale* 6 (2014) 2009–2026.
- [16] B. Xu, Y. An, Y. Liu, X. Qin, X. Zhang, Y. Dai, Z. Wang, P. Wang, M.-H. Whangbo, B. Huang, Enhancing the photocatalytic activity of BiOX (X=Cl, Br, and I), (BiO)<sub>2</sub>CO<sub>3</sub> and Bi<sub>2</sub>O<sub>3</sub> by modifying their surfaces with polar organic anions, 4-substituted thiophenolates, *J. Mater. Chem. A* 5 (2017) 14406–14414.
- [17] J. Tian, Z. Chen, J. Jing, C. Feng, M. Sun, W. Li, Enhanced photocatalytic activity of BiOCl with regulated morphology and band structure through controlling the adding amount of HCl, *Mater. Lett.* 272 (2020) 127860.
- [18] J. Xia, J. Di, H. Li, H. Xu, H. Li, S. Guo, Ionic liquid-induced strategy for carbon quantum dots/BiOX (X=Br, Cl) hybrid nanosheets with superior visible light-driven photocatalysis, *Appl. Catal. B Environ.* 181 (2016) 260–269.
- [19] S. Lei, D. Cheng, X. Gao, L. Fei, W. Lu, J. Zhou, Y. Xiao, B. Cheng, Y. Wang, H. Huang, A new low-temperature solution route to Aurivillius-type layered oxyfluoride perovskites Bi<sub>2</sub>MO<sub>3</sub>F (M= Nb, Ta) as photocatalysts, *Appl. Catal. B Environ.* 205 (2017) 112–120.
- [20] X. Jia, Q. Han, X. Wang, J. Zhu, Milling-induced synthesis of BiOCl<sub>1-x</sub>Br<sub>x</sub> solid solution and their adsorptive and photocatalytic performance, *Photochem. Photobiol.* 94 (2018) 942–954.
- [21] Q.Y. Liu, G. Han, Y.F. Zheng, X.C. Song, Synthesis of BiOBr<sub>x</sub>I<sub>1-x</sub> solid solutions with dominant exposed {0 0 1} and {1 1 0} facets and their visible-light-induced photocatalytic properties, *Sep. Purif. Technol.* 203 (2018) 75–83.
- [22] Z. Shan, W. Wang, X. Lin, H. Ding, F. Huang, Photocatalytic degradation of organic dyes on visible-light responsive photocatalyst PbBiO<sub>2</sub>Br, *J. Solid State Chem.* 181 (2008) 1361–1366.
- [23] J. Tian, Z. Chen, X. Deng, Q. Sun, Z. Sun, W. Li, Improving visible light driving degradation of norfloxacin over core-shell hierarchical BiOCl microspherical photocatalyst by synergistic effect of oxygen vacancy and nanostructure, *Appl. Surf. Sci.* 453 (2018) 373–382.
- [24] L. Ye, L. Zan, L. Tian, T. Peng, J. Zhang, The {001} facets-dependent high photoactivity of BiOCl nanosheets, *Chem. Commun.* 47 (2011) 6951–6953.
- [25] B. Wang, J. Di, P. Zhang, J. Xia, S. Dai, H. Li, Ionic liquid-induced strategy for porous perovskite-like PbBiO<sub>2</sub>Br photocatalysts with enhanced photocatalytic activity and mechanism insight, *Appl. Catal. B Environ.* 206 (2017) 127–135.
- [26] H.-Y. Hao, Y.-Y. Xu, P. Liu, G.-Y. Zhang, BiOCl nanostructures with different morphologies: Tunable synthesis and visible-light-driven photocatalytic properties, *Chin. Chem. Lett.* 26 (2015) 133–136.
- [27] Y. Zhang, X. Chen, F. Jiang, Y. Bu, J.-P. Ao, BiVO<sub>4</sub> photoanode modification by In-doping and anoxic annealing by synergistic regulation, *ACS Sustain. Chem. Eng.* 8 (2020) 9184–9194.
- [28] X. Zhong, H. He, M. Yang, G. Ke, Z. Zhao, F. Dong, B. Wang, Y. Chen, X. Shi, Y. Zhou, In<sup>3+</sup>-doped BiVO<sub>4</sub> photoanodes with passivated surface states for photoelectrochemical water oxidation, *J. Mater. Chem. A* 6 (2018) 10456–10465.
- [29] J. Hu, W. Fan, W. Ye, C. Huang, X. Qiu, Insights into the photosensitivity activity of BiOCl under visible light irradiation, *Appl. Catal. B Environ.* 158 (2014) 182–189.
- [30] S. Yin, J. Di, M. Li, Y. Sun, J. Xia, H. Xu, W. Fan, H. Li, Ionic liquid-assisted synthesis and improved photocatalytic activity of p-n junction g-C<sub>3</sub>N<sub>4</sub>/BiOCl, *J. Mater. Sci.* 51 (2016) 4769–4777.
- [31] H. Lu, L. Xu, B. Wei, M. Zhang, H. Gao, W. Sun, Enhanced photosensitization process induced by the p-n junction of Bi<sub>2</sub>O<sub>3</sub>CO<sub>3</sub>/BiOCl heterojunctions on the degradation of rhodamine B, *Appl. Surf. Sci.* 303 (2014) 360–366.
- [32] J. Xia, S. Yin, H. Li, H. Xu, L. Xu, Y. Xu, Improved visible light photocatalytic activity of sphere-like BiOBr hollow and porous structures synthesized via a reactable ionic liquid, *Dalton Trans.* 40 (2011) 5249–5258.
- [33] M.-Y. Hsu, H.-L. Hsu, J. Leu, TiO<sub>2</sub> nanowires on anodic TiO<sub>2</sub> nanotube arrays (TNWs/TNAs): formation mechanism and photocatalytic performance, *J. Electrochem. Soc.* 159 (2012) H722–H727.
- [34] M. Chen, W. Chu, Efficient degradation of an antibiotic norfloxacin in aqueous solution via a simulated solar-light-mediated Bi<sub>2</sub>WO<sub>6</sub> process, *Ind. Eng. Chem. Res.* 51 (2012) 4887–4893.
- [35] U. Neugebauer, A. Szeghalmi, M. Schmitt, W. Kiefer, J. Popp, U. Holzgrabe, Vibrational spectroscopic characterization of fluoroquinolones, *Spectrochim. Acta Part A Mol. Biomol. Spectrosc.* 61 (2005) 1505–1517.
- [36] X. Zhang, J. Wei, R. Li, C. Zhang, H. Zhang, P. Han, C. Fan, DFT+U predictions: structural stability, electronic and optical properties, oxidation activity of BiOCl photocatalysts with 3d transition metals doping, *J. Mater. Sci.* 53 (2018) 4494–4506.